GEOPHYSICS, VOL. 81, NO. 4 (JULY-AUGUST 2016); P. M55–M69, 13 FIGS., 2 TABLES.
10.1190/GEO2015-0492.1

Estimation of rock physics properties from seismic attributes — Part 2: Applications

Bastien Dupuy[1], Stéphane Garambois[2], Amir Asnaashari[3], Hadi M. Balhareth[4], Martin Landrø[4], Alexey Stovas[4], and Jean Virieux[2]

ABSTRACT

The estimation of quantitative rock physics properties is of great importance for reservoir characterization and monitoring in CO_2 storage or enhanced oil recovery as an example. We have combined the high-resolution results of full-waveform inversion (FWI) methods with rock physics inversion. Because we consider a generic and dynamic rock physics model, our method is applicable to most kinds of rocks for a wide range of frequencies. The first step allows determination of viscoelastic effective properties, i.e., quantitative seismic attributes, whereas the rock physics inversion estimates rock physics properties (porosity, solid frame moduli, fluid phase properties, or saturation). This two-step workflow is applied to time-lapse synthetic and field cases. The sensitivity tests that we had previously carried out showed that it can be crucial to use multiparameter inputs to accurately recover fluid saturations and fluid properties. However, due to the limited data availability and difficulties in getting reliable multiparameter FWI results, we are limited to acoustic FWI results. The synthetic tests are conclusive even if they are favorable cases. For the first time-lapse fluid substitution synthetic case, we first characterize the rock frame parameters on the baseline model using P-wave velocity estimations obtained by acoustic FWI. Then, we obtain an accurate estimation of fluid bulk modulus from the time-lapse P-wave velocity. In the Marmousi synthetic case, the rock frame properties are accurately recovered for the baseline model, whereas the gas saturation change in the monitor model is not estimated correctly. On the field data example (time-lapse monitoring of an underground blowout in the North Sea), the estimation of rock frame properties gives results on a relatively narrow range, and we use this estimation as a starting model for the gas saturation inversion. We have found that the estimation of the gas saturation is not accurate enough, and the use of attenuation data is then required. However, the uncertainty on the estimation of baseline rock frame properties is not critical to monitor gas saturation changes.

INTRODUCTION

Quantitative interpretation in active seismic exploration has steadily improved in the past few decades. High-resolution seismic reflection methods are used for subsurface structure characterization, but quantitative methods are essential to obtain quantitative acoustic, elastic, or viscoelastic properties in complex heterogeneous media. Full-waveform inversion (FWI) methods are the last improvement of these seismic imaging methods and can provide high-resolution images of effective seismic attributes. As an example, acoustic properties (Sirgue et al., 2009), multiparameter elastic and anisotropic properties (Prieux et al., 2013a, 2013b), and attenuations (Malinowski et al., 2011) are now obtained from FWI with a vertical resolution of a half-wavelength (Sirgue and Pratt, 2004) and even better for lateral resolution. This work presents a strategy to estimate rock physics properties by inverting the effective medium properties derived from FWI. The poroelastic FWI-like method is very difficult to implement because of the computational cost and the large trade-off between poroelastic properties (De Barros and Dietrich, 2008; Morency et al., 2009; De Barros

Manuscript received by the Editor 17 September 2015; revised manuscript received 16 February 2016; published online 14 June 2016.
[1]Formerly ISTerre, Grenoble, France and NTNU, Trondheim, Norway; presently SINTEF Petroleum Research, Trondheim, Norway. E-mail: bastien.dupuy@sintef.no.
[2]Université Grenoble Alpes, ISTerre, CNRS UMR 5275, Grenoble, France. E-mail: stephane.garambois@ujf-grenoble.fr; jean.virieux@ujf-grenoble.fr.
[3]Formerly ISTerre, Grenoble, France and DanaEnergy, Tehran, Iran; presently PGS Exploration, Weybridge, UK. E-mail: amir.asnaashari@ujf-grenoble.fr.
[4]NTNU, Trondheim, Norway. E-mail: hadi.m.balhareth@ntnu.no; martin.landro@ntnu.no; alexey.stovas@ntnu.no.

et al., 2010). Consequently, we choose to use a two-step inverse approach: (1) from viscoelastic seismic attributes (velocities and quality factors) determined by a first inversion step and (2) we recover rock physics parameters by an inversion process, which is described by Dupuy et al. (2016b).

This two-step concept has first been proposed by Berkhout and Wapenaar (1990) and applied by Saltzer et al. (2005). Calibrating the inversions by well prior information, they use seismic reflection data to estimate rock physics properties (shale volume and porosity). This method does not require statistically significant sampling of reservoir properties, which is a major advantage over empirical approaches (Mavko et al., 2009). In addition, the fluid effects are determined from well data, so the porosity and lithology effects do not interfere with fluid effects. Otherwise, a discrimination would be needed using only P- and S-impedances. Nevertheless, in addition to the limitation related to the use of reflection data, Saltzer et al. (2005) use Gassmann equations (Gassmann, 1951) to define the rock physics model and consequently are limited to low-frequency approximations. On the other hand, they use conventional seismic inversion, which mostly uses the reflectivity data for inversion, whereas FWI uses refraction and reflection data. Seismic inversion generally suffers from the lack of low frequency content of the seismic reflectivity data. However, FWI technique that uses refraction and wide-aperture data can recover the low wavenumber part (low-frequency information) of velocity model (Qureshi et al., 2012). Therefore, FWI results can be more accurate at low frequencies and can provide higher resolution image as well.

A similar approach is also used by Chotiros (2002) for water-saturated sands. He shows that fitting the seismic data using viscoelastic models is not accurate due to porous waves conversions, which are not considered in the modeling. Then, he includes a poroelastic model for his inversion, that helps to deduce the dry bulk modulus K_D and the dry shear modulus G_D from P- and S-wave velocities and attenuations (V_P, V_S, Q_P, and Q_S). He also proposes some improvements in the accuracy of estimation by introducing more complex models (composite materials or porosity variation with fluid pressure). Based on seismic attributes and amplitude variation with offset (AVO) data, Johansen et al. (2013) develop an inverse modeling method to predict lithology and reservoir quality. Using the same workflow, Moyano et al. (2015) insist on the nonuniqueness of the inversion and the needs of spatial correlation constrains. Nevertheless, these works are mainly based on well-log data and qualitative seismic attributes. Grude et al. (2014) estimate pressure and saturation using amplitude variations of time-lapse seismic data. In this paper, we do not consider pore pressure or stress effects.

In addition to the use of a Biot dynamic poroelasticity theory (Dupuy et al., 2016b), our work relies on the use of high-resolution quantitative data, derived with FWI techniques. Inverted seismic attributes are generally limited to P- and S-wave velocities, extracted from seismograms using arrival-time tomography. The use of FWI offers the possibility of an enhanced accuracy and resolution for velocities and quality factors estimations (Malinowski et al., 2011), as amplitudes are considered in the inversion process. In addition, considering an elastic approximation for FWI allows to use S-waves, which is crucial for several main reasons:

1) It allows to include the whole seismic data set that is important because the rock physics inversion system is highly underdetermined.
2) The effects of nonfluid parameters (porosity, compaction, clay content, etc.) on V_P and V_S are similar, but fluids have different effects on V_P and V_S (Berryman et al., 2002; Avseth et al., 2005).
3) The sensitivity tests carried out by Dupuy et al. (2016b) show that using more than one input data helps to constrain the poroelastic inversion. In addition, parameters such as saturation and permeability cannot be estimated without attenuation input data. On the other hand, the discrimination of fluid effects (pressure and saturation) requires S-waves in addition to P-waves.

Pioneer works on FWI techniques show that density is difficult to reconstruct realistically (Forgues and Lambaré, 1997; Choi et al., 2008) with short-offset data. Using wide-aperture data and considering the coupled inversion of velocities and impedances can help to discriminate the effects of velocity and density. The ill-posedness of the multiparameter FWI problem makes the estimation of attenuation properties difficult as well. Despite of some applications at various scales (Liao and McMechan, 1995; Hicks and Pratt, 2001; Malinowski et al., 2011), due to the coupling of V_P and Q_P (Ribodetti et al., 2000), Kamei and Pratt (2013) recommend to invert sequentially V_P and then Q_P. Similar sequential strategies are also proposed for elastic FWI (Tarantola, 1986; Sears et al., 2008). Brossier et al. (2009) define efficient data preconditioning to deal with strong surface waves energy, whereas Shi et al. (2007) parameterize the inversion with Lamé parameters and Poisson's ratio to successfully detect thin gas layers. Romdhane et al. (2011) confirm the difficulties of dealing with surface waves for near-surface data and propose some applications of elastic FWI for landslides. Prieux et al. (2013a, 2013b) test several parameterizations and illustrate the difficulties of full viscoelastic FWI on field data, which relies on accurate initial models and wide-aperture data. Ren et al. (2014) (for viscoacoustic problems) and Ren and Liu (2015) (for elastic problems) propose several strategies to reduce the computational cost (with variable operator lengths) and the ill-posedness (with second generation wavelet transform) of the multiparameter FWI. Operto et al. (2013) sum up the recent advances in multiparameter FWI and illustrate the complexity of the choice of the most efficient parameterization.

Because the FWI approach delivers high-resolution quantitative images of macroscale physical parameters, it could be used as an attractive technique for monitoring purposes (Gosselet and Singh, 2008; Plessix et al., 2010; Romdhane and Querendez, 2014). QueiBer and Singh (2013) apply acoustic time-lapse FWI to Sleipner CO_2 storage data. They correlate V_P changes with CO_2 saturation changes but they use a simplistic effective fluid phase model. However, several studies such as acoustic time-lapse FWI considering prior information (Asnaashari et al., 2015) and robust simultaneous time-lapse FWI (Maharramov and Biondi, 2015) have been done to demonstrate how to better improve the reconstruction of time-lapse model changes, there is still an active research in this direction. Improving the accuracy of macroscale time-lapse FWI model has a direct impact on the sensitivity of microscale models (Dupuy et al., 2016a). Raknes et al. (2015) apply elastic FWI to Sleipner 3D data but the S-wave velocities and the densities are coupled to V_P and not directly inverted, which is not reliable when fluid effects are present. As the developments toward multiparameter FWI are still under progress and not widely applied to real data, we have restricted our analysis to acoustic FWI results. However, considering acoustic FWI results also allow to take advantage

of the high-resolution results provided by Balhareth and Landrø (2015) or Romdhane and Querendez (2014) (up to 40 Hz).

In this paper, after a quick reminder about the method defined in Dupuy et al. (2016b), we apply the process to synthetic and field data cases. All applications deal with monitoring cases, which allow to reduce the uncertainty on a priori rock physics properties and to take advantage of the time-lapse data redundancy to focus on the fluid changes estimates. First, we use time-lapse FWI results to invert fluid properties in a layered reservoir. The second synthetic test deals with well-known Marmousi model, in which fluid saturation changed. Finally, we apply the process to field data acquired in the North Sea where a blowout occurred, and we estimate the gas saturation change due to this blowout. We decided to use acoustic data and then to use only P-wave velocity as input data for the rock physics inversion. This choice is driven by simplicity's sake and because current FWI techniques still struggle to obtain satisfying high-resolution multiparameters inversion.

METHODS

Forward modeling

The forward modeling requires the definition of a rock physics model linking the poroelastic properties to viscoelastic attributes via a homogenization process. We choose to use the generic model defined by Pride (2005), which combined classical Biot-Gassmann theories with a generalized dynamic permeability (Johnson et al., 1987). The full rock physics model is described by Dupuy et al. (2016b). The complex slownesses of P- and S-waves (s_P and s_S) are given by

$$s_P^2 = \frac{\gamma}{2} - \frac{1}{2}\sqrt{\gamma^2 - \frac{4(\rho\tilde{\rho} - \rho_f^2)}{HM - C^2}}, \quad s_S^2 = \frac{\rho - \rho_f^2/\tilde{\rho}}{G}, \tag{1}$$

where γ and H are

$$\gamma = \frac{\rho M + \tilde{\rho} H - 2\rho_f C}{HM - C^2}, \qquad H = K_U + \frac{4}{3}G. \tag{2}$$

The mean density ρ, the fluid density ρ_f, and the flow resistance $\tilde{\rho}$ are the three inertial terms, whereas the undrained bulk modulus K_U, the shear modulus G, the Biot modulus C, and the fluid storage coefficient M are the four mechanical moduli. These seven parameters are derived by the homogenization process and describe the macroscale state (wavelength scale) of the porous medium (Pride, 2005; Dupuy et al., 2011). Considering biphasic fluids requires the computation of an effective fluid phase. The combination of the properties of the two fluids (bulk modulus, viscosity, and density) allows us to compute an effective fluid phase that is plugged into the saturated Biot theory. We use advanced averages (the Brie et al. [1995] approximation for the bulk modulus, the Teja and Rice [1981] approximation for the viscosity and arithmetic average for density) which have been shown to fit well real data if there is uniform saturation. If patchy saturation is considered (White, 1975), an advanced dynamic theory including frequency-dependent effective moduli is used (Pride et al., 2004).

The effective viscoelastic velocities and quality factors for P- and S-waves are deduced:

$$V_{P,S}(\omega) = \frac{1}{\mathrm{Re}(s_{P,S}(\omega))}. \quad Q_{P,S}(\omega) = \frac{\mathrm{Re}(s_{P,S}^2(\omega))}{\mathrm{Im}(s_{P,S}^2(\omega))}. \tag{3}$$

The viscoelastic velocities (V_P and V_S), quality factors (Q_P and Q_S), and the mean density ρ are the input data of our rock physics inverse problem.

Rock physics inversion method

The inverse problem consists of the extraction from input data (seismic attributes deduced from seismograms) of models (poroelastic parameters) and is formulated as

$$\boldsymbol{d} = g(\boldsymbol{m}), \tag{4}$$

where $\boldsymbol{d}$ is the data vector, $\boldsymbol{m}$ is the model vector, and g is a nonlinear function linking models and data. In our approach, the function g contains the analytical Biot-Gassmann relations, which compute P- and S-waves velocities and quality factors as well as the density. The forward model computation is very fast, and the number of model parameters is low. We use an oriented Monte-Carlo method (neighborhood algorithm introduced by Sambridge, 1999), which is based on random exploration but is guided toward best models to reduce computational costs. The optimization aims to minimize a scalar function (misfit function) describing the discrepancy between the observed data $\boldsymbol{d}_{obs}$ and the calculated data $g(\boldsymbol{m})$ (by forward modeling). We use a L_2 norm to compute the misfit $C(\boldsymbol{m})$ as

$$C(\boldsymbol{m}) = \frac{1}{2}[(\boldsymbol{d}_{obs} - g(\boldsymbol{m}))^T(\boldsymbol{d}_{obs} - g(\boldsymbol{m}))]. \tag{5}$$

Summary of sensitivity analysis

Dupuy et al. (2016b) show the sensitivity analysis of the rock physics inversion method. Several combinations of input parameters and inverted models are tested and the conclusions are

1) The inversion system should be well-determined; i.e., the number of input data should be equal or higher than the number of poroelastic models.
2) Consequently, using appropriate assumptions on some poroelastic phases, a selection of several well-chosen inverted parameters can be done.
3) The estimation of rock frame moduli and porosity and the estimation of saturating fluid properties are accurate using P- and S-waves velocities data.
4) The estimation of permeability and fluid saturation requires attenuation data.
5) The uncertainty related to a priori assumptions or related to input data linearly shift the estimation but not dramatically.

Workflow

The two-step workflow described in the "Introduction" section (FWI plus rock physics inversion) is applied to three test cases. For both of synthetic cases, we compute acoustic seismic data sets. These data sets are used to compute acoustic velocity using FWI. The acoustic velocity is then used to estimate several rock physics

properties. This workflow is applied in a time-lapse way, for baseline and monitor models, considering some fluid changes. For the field data case, we have a slightly different approach because we have less a priori information. Consequently, the rock physics inversion is focused toward the area of interest, i.e., one of the sand layers in which the gas has migrated. It allows us to underline more the uncertainties of rock physics inversion and especially for the estimation of the saturation.

FLUID SUBSTITUTION IN A LAYERED RESERVOIR

Model description

This realistic case is based on Dai et al. (1995) synthetic example and consists of an oil reservoir in which steam is injected to improve the oil recovery. Eight horizontal sand layers, in which the degree of consolidation increases with depth, are defined by their poroelastic parameters (Table 1). The fluid phase saturating the porous medium consists of water except for the reservoir layer (layer number 6), saturated only with oil before the injection. During the steam injection, two concentric half-circles are created around the injection point (the top of the reservoir layer) where the porous medium becomes saturated with steam and heated oil, respectively. These changes in fluid properties affect the viscoelastic seismic parameters (velocities and attenuations) (given in Table 1).

Figure 1 shows the true baseline and monitor models for the considered poroelastic and seismic parameters, respectively, the porosity and P-wave velocity for the baseline model, and the fluid properties and the P-wave velocity for the monitor model. The other poroelastic and viscoelastic parameters are given in Table 1. The porosity ϕ (Figure 1b) decreases with depth, except in the reservoir layer where it is higher. The fluid phase parameters are constant in each layer (water) except in the sixth one, saturated with oil for the baseline model (Figure 1d–1f). After injection, we can easily observe the two concentric half-circles for steam and heated oil phases in the reservoir layer. The corresponding acoustic velocities are given for the baseline and monitor models. Overall, V_P increases with depth (related to the porosity and rigidity values), except in the high porosity reservoir layer, which presents velocities lower than overburden layers (Figure 1a). The fluid phase change in the reservoir also has a large impact on V_P values (Figure 1c).

FWI results

The acoustic seismograms computed from the baseline V_P model (Figure 1a) are generated using acoustic finite-difference modeling in the time domain with a fourth-order stencil in space and a second-order integration in time (Levander, 1988). From these data (Figure 2), FWI is performed in the time domain (Mora, 1987, 1989) and gives a high-resolution estimation of acoustic velocities. The source and receiver layout is

1) There are 22 sources every 25 m on a horizontal line at a 75 m depth.
2) There are 45 receivers on this horizontal line and 45 receivers in two vertical wells located at the end of the horizontal line ($x = 75$ m and $x = 625$ m). The receivers are separated by 12.5 m intervals.

Table 1: Poroelastic and viscoelastic parameters of the Dai reservoir model (coming from Dai et al., 1995). The velocities and the quality factors of P- and S-waves (V_P, V_S, Q_P, and Q_S) are computed for the central frequency of the seismic source (20 Hz).

			Sand layers							Reservoir layer (6)		
			1	2	3	4	5	7	8	Oil	Steam	Heated oil
Poroelastic parameters	K_s	(GPa)	5.2	5.3	5.8	7.5	6.9	9.4	26	37	37	37
	G_s	(GPa)	2.4	2.9	3.3	4.2	3.6	5.6	17	4.4	4.4	4.4
	ρ_s	(kg/m^3)	2250	2300	2400	2490	2211	2670	2700	2650	2650	2650
	K_f	(GPa)	2.5	2.5	2.5	2.5	2.5	2.5	2.5	1.7	0.0014	1.2
	ρ_f	(kg/m^3)	1040	1040	1040	1040	1040	1040	1040	985	10	900
	η	(Pa.s)	0.001	0.001	0.001	0.001	0.001	0.001	0.001	150	2.2×10^{-5}	0.3
	m		1.5	1.5	1.5	1.5	1.5	1.5	1.5	1.5	1.5	1.5
	K_D	(GPa)	0.65	1.59	2.76	4.54	5.69	6.58	12.35	3.21	3.21	3.21
	ϕ		0.25	0.1	0.05	0.03	0.01	0.02	0.05	0.33	0.33	0.33
	k_0	(m^2)	10^{-12}	10^{-13}	10^{-13}	10^{-13}	10^{-16}	10^{-13}	10^{-14}	10^{-12}	10^{-12}	10^{-12}
Viscoelastic parameters	V_P	(m/s)	1505	1613	1749	2019	2179	2265	3281	1900	1428	1768
	V_S	(m/s)	330	548	733	936	1116	1140	1571	359	390	361
	Q_P		948	413	$+\infty$	1054	$+\infty$	$+\infty$	$+\infty$	$+\infty$	$+\infty$	$+\infty$
	Q_S	$\times 10^3$	14.33	160	172	180	1.62×10^5	194	1925	2.58×10^6	3114	6108
	ρ	(kg/m^3)	1948	2174	2332	2445	2200	2637	2617	2100	1779	2073

The data are generated with an isotropic source consisting of a Ricker wavelet centered at 20 Hz. The seismograms obtained for a source centered on the horizontal line are shown in Figure 2 before and after the steam injection. The reflected P-waves generated at the top of the reservoir (PP5) and at the substratum (PP7) are visible in each seismogram. Amplitudes of the reflected P-waves coming from the reservoir layer are different before and after injection. The vertical well receivers allow to complete the wavenumber spectrum by improving the illumination, and it is similar to the case when a long offset is recorded. Then, we perform the acoustic FWI in the time domain, involving all the frequency components of the source wavelet, to invert the acoustic data set. Two FWI are performed to first recover precisely the baseline model (Asnaashari et al., 2011, 2013) and second, to detect time-lapse changes with a differential approach (Asnaashari et al., 2015). The starting model for the baseline is a smooth version of the true model (Asnaashari et al., 2011).

Baseline model results

Using the acoustic velocity obtained from FWI carried on baseline model as input data, a rock physics estimation is performed for each pixel using the inversion algorithm presented by Dupuy et al. (2016b). The acoustic FWI delivers a high-resolution map of V_P values (Figure 3b). Including the prior model information into FWI allows inversion to converge toward the true V_P model (Figure 1a). For more information about baseline model reconstruction using a prior model, refer to Asnaashari et al. (2013).

The quality of the rock physics inversion results is directly related to the resolution obtained for the viscoelastic seismic attributes. Here, we want to recover the frame parameters for the baseline model because we assume that we know the lithology and the fluid phase (thanks to log data). The sensitivity tests show that we can invert directly the porosity from only P-wave velocity data (Dupuy et al., 2016b). Therefore, from V_P data recovered by acoustic FWI (Figure 3b), we obtain very good results for porosity (Figure 3a to be compared with the true model in Figure 1b).

Monitor model results

After the characterization of the baseline medium, a double-difference FWI based on the inversion of the difference between baseline and monitor data sets (Watanabe et al., 2004; Denli and Huang, 2009) is performed (Asnaashari et al., 2015). We obtain then a V_P model after injection in which the fluid change in the reservoir layer is clearly visible. For the rock physics inversion, we assume that we know a priori the overburden properties determined by the previous step on the baseline medium and we invert only the fluid properties in the reservoir layer: bulk modulus K_f, viscosity η, and density ρ_f.

According to the sensitivity analysis (Dupuy et al., 2016b), from V_P only, we can estimate pretty well K_f. The results show that η (Figure 4a) and ρ_f (Figure 4b) are poorly constrained and estimated, but the K_f inversion (Figure 4c) is good. More precisely, for the inner half-circle (saturated with steam), most of the estimated values are below 0.03 GPa (the highest value is 0.63 GPa, and the smallest value is 0.013 GPa). The exact value for the steam is $K_f = 0.0014$ GPa. For the outer half-circle, the values are between 0.97 and 1.6 GPa, whereas the exact value is $K_f = 1.2$ GPa for the heated oil. For the heated oil, the values are close to the true one, with 30% of uncertainty, whereas for the steam, the values are one

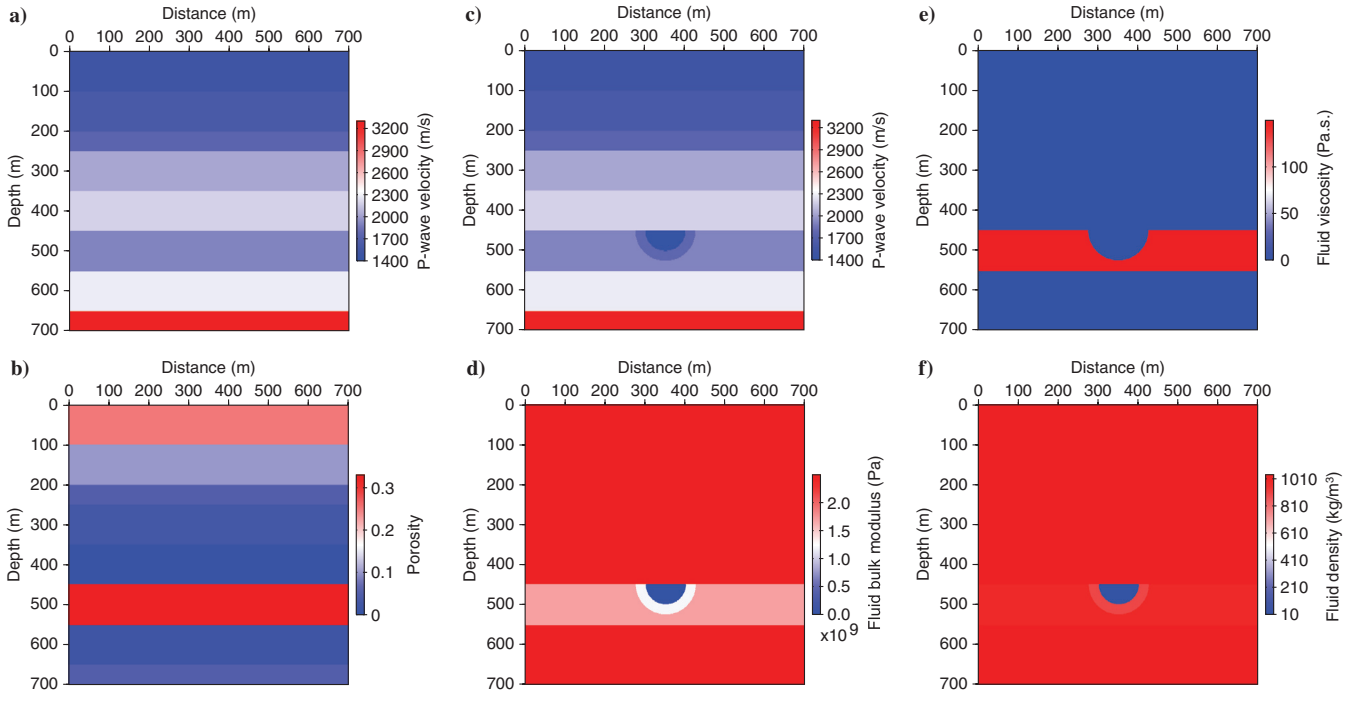

Figure 1. Baseline (before injection, a and b) and monitor (after injection, c-f) true models: (a) V_P, (b) ϕ, (c) V_P, (d) K_f, (e) η, and (f) ρ_f. The others poroelastic and viscoelastic properties are given in Table 1. We give only the properties varying in this application: only P-wave velocities will be estimated from FWI, whereas porosity (baseline) and fluid properties (monitor) will be derived using the rock physics inversion method.

order of magnitude too high but are significantly lower than common values for liquids (oil, water, and so on), so it allows to identify clearly the gas phase. In addition, the geometric distribution of these fluids (concentric half-circles) is clearly visible. Moreover, as the bulk modulus values are well-estimated, we can determine the fluid nature even if the two other parameters are not recovered.

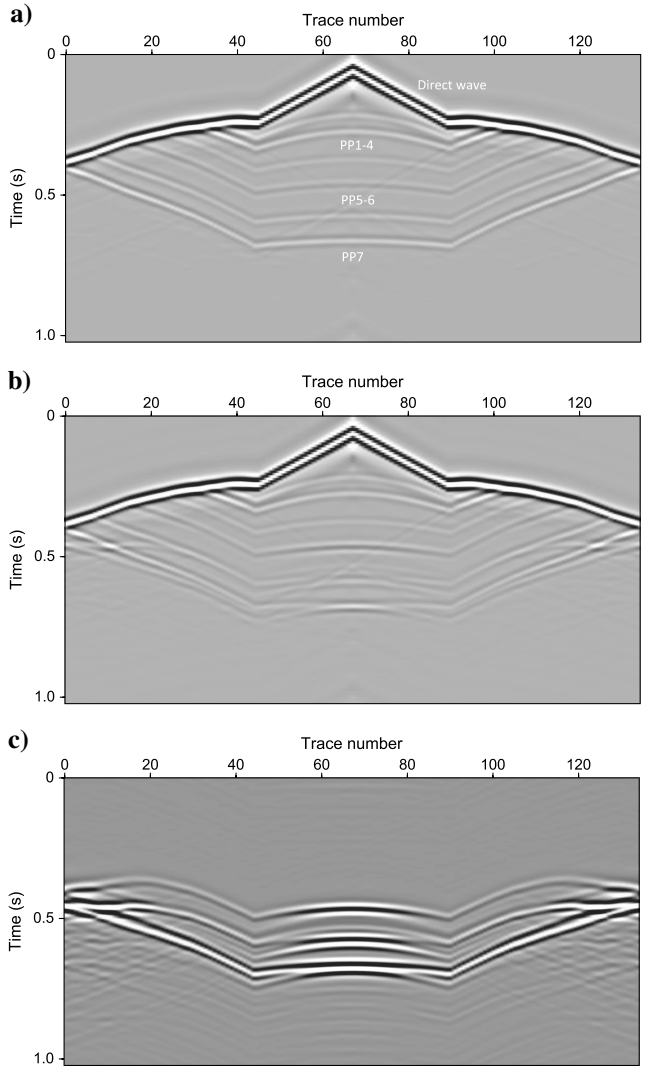

Figure 2. Seismograms obtained for a source at 250 m from the side of the acquisition layout. Simulations for the (a) baseline model and (b) monitor model and (c) differential seismogram. The differential seismogram traces are multiplied by a factor 10 for visualization purpose. Trace numbers 46–90 correspond to the receivers set on the horizontal line ($z = 75$ m deep, 75 m $< x <$ 625 m), trace numbers 1–45 correspond to the receivers set in the left well ($x = 75$ m deep, 75 m $< z <$ 625 m), and trace numbers 91–135 correspond to the receivers set in the right well ($x = 625$ m deep, 75 m $< z <$ 625 m). The reflection events are labeled from 1 to 7 with respect to the layer interfaces (PP1 is the reflection between first and second layers, PP2 is the reflection between second and third layers, and so on. PP5 is the reflection at the top of the reservoir). The effect of the fluid change in the reservoir is clearly visible on the differential data (PP5).

TIME-LAPSE MONITORING IN THE MARMOUSI MODEL

Model description

The second realistic example is based on a part of the well-known synthetic Marmousi model (Martin et al., 2006). We use the noise-free and noisy results of Asnaashari et al. (2013) for the baseline models and results of Asnaashari et al. (2015) for the monitor models. The Marmousi model is defined by effective elastic properties given in Figure 5 (Martin et al., 2006). To define the poroelastic properties, we assume that the main part of the model is constituted by shales (75% of silica and 25% of clay) and the reservoir layers by sandstones (see Figure 5). The associated grain properties are computed from Bourbié et al. (1986) and Mavko et al. (2009) and are given in Table 2 and Figure 5d. All layers are saturated by water except the two reservoirs saturated with gas (Figure 5e). The value of fluid phase properties is given in Table 2 and computed from Batzle and Wang (1992) and Mavko et al. (2009).

FWI results

Similarly to the previous example, we use an acoustic finite-difference modeling in the time domain to compute the acoustic synthetic data. We consider 77 isotropic explosive sources, located along a horizontal line at a depth of 16 m, equally spaced by a distance of 50 m. A horizontal receiver line at a depth of 15 m with an interval of 10 m completes the acquisition layout. An explosive source (Ricker wavelet source with a central frequency of 10 Hz) is used, for baseline and monitor surveys. The seismograms

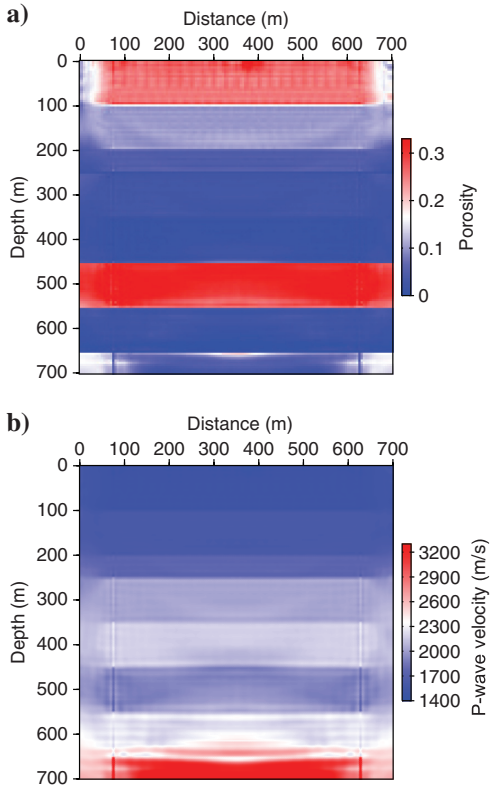

Figure 3. Inversion of porosity ϕ (a) from V_P data (b) estimated by acoustic FWI.

for a central source position are given for noise-free and noisy examples in Figure 6 for baseline and monitor models. The synthetic seismograms show multiple reflections due to the free-surface conditions. It is worth noting that the time-lapse signal is weak and even blinded in the case of noisy data. The initial P-wave velocity model is a smooth version of the true model (Asnaashari et al., 2015).

Baseline model results

For the baseline model, we assume that the prior rock physics parameters are the solid phase (sands or shales) properties (bulk K_s and shear G_s moduli of grains and grains density ρ_s; see Table 2 and Figure 5d) and the saturating fluid phase (water or gas) properties (fluid bulk modulus K_f, viscosity η, and density ρ_f; see Table 2 and Figure 5e). We invert only the frame properties (porosity ϕ, drained bulk modulus K_D, and drained shear modulus G_D). The input P-wave velocity is inverted from noise-free (Figures 7 and 8) and noisy data (Figure 9).

Figure 7 shows the result of the rock physics inversion using V_P result obtained from FWI on noise-free data. The rock frame properties are not very well-estimated, which is consistent with the sensitivity tests performed in Dupuy et al. (2016b). The inversion system is strongly underdetermined (only one input data for three inverted parameters). Nevertheless, the main trends (decrease of porosity with depth and increase of mechanical moduli with depth) and the main structures are visible. To figure out the input related to elastic data, we carry out the rock physics inversion using the true models for S-wave velocity and density (Figure 5) in addition to the V_P input data from FWI. Figures 8 and 9 show the ϕ, K_D, and G_D inversion results considering elastic input data. The FWI V_P results are inverted from noise-free and noisy data, respectively. Using the additional constrains coming from V_S and ρ help to obtain very accurate results for each rock physics properties. The results for noise-free and noisy data are similar, the sharpness is being a bit better for noise-free data at large depths. The porosity and bulk modulus results are highly related to the V_P data, with smoother variations at high depth. The shear modulus result is mainly related to the true V_S data and so contains really sharp structures. However, ϕ, K_D, and G_D results give accurate structures and realistic values. It is worth noting that only the porosity values are bounded during the poroelastic inversion (between 0 and 0.4), whereas K_D and G_D values are free.

Some additional tests about the estimation of frame properties from different input have been performed (results not shown here). Using only a smooth V_P model (initial model of FWI which could be obtained by traveltime tomography) as input data, the quality of frame parameters estimation results is damaged. The main structures are not visible, only the two reservoirs appear on the images (but with a lower porosity than the overburden). In addition to smooth V_P model, if we use true V_S and density models, the images of frame parameters show clearly the structures and layers. But, the values of porosity and bulk modulus are quite different from those estimated with high-resolution V_P (Figure 8). The conclusion is that the smooth V_P data are not constraining ϕ and K_D estimates. But,

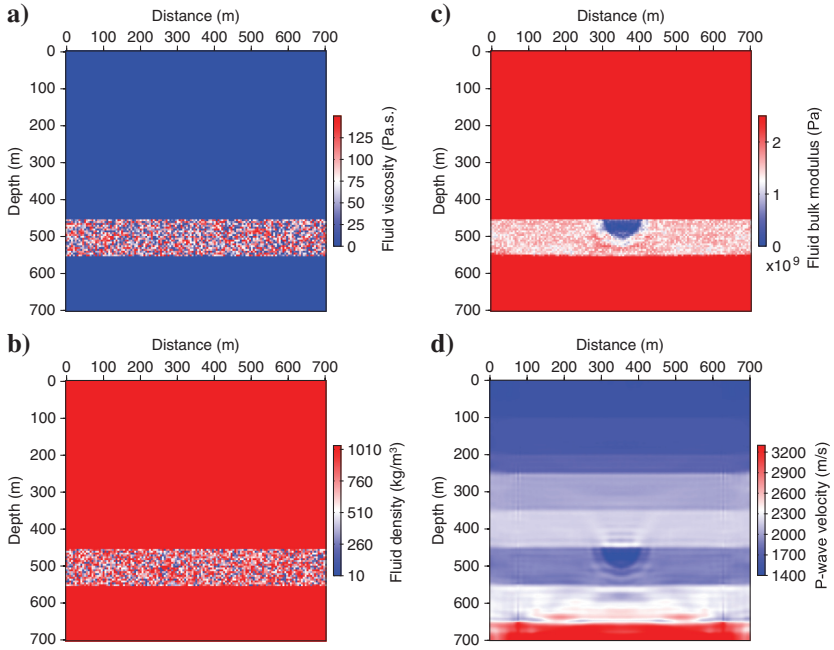

Figure 4 : Inversion of poroelastic parameters of the fluid phase (a) η, (b) ρ_f (c) K_f from V_P data (d) estimated by acoustic inversion.

Table 2. Poroelastic and viscoelastic parameters used in the Marmousi model. The values for sandstone and shale are defined using silica and clay grain properties (Bourbié et al., 1986; Mavko et al., 2009). The properties of the fluid phases are taken from Batzle and Wang (1992) and Mavko et al. (2009). The propagation velocities and densities of C2 and C3 reservoirs are defined in Martin et al. (2006). The values of K_D, G_D, and ϕ are inverted at 10 Hz.

		Sandstone	Shale
K_s	(GPa)	37	28
G_s	(GPa)	44	14
ρ_s	(kg/m^3)	2700	2635
m		1	1
k_0	(m^2)	10^{-13}	10^{-13}
		Brine	Gas
K_f	(GPa)	3.01	0.13
ρ_f	(kg/m^3)	1055	336
η	(Pa.s)	0.001	0.00004
		C2 reservoir	C3 reservoir
V_P	(m/s)	2131	1584
V_S	(m/s)	1209	881
ρ	(kg/m^3)	1860	1720
ϕ		0.355	0.415
K_D	(GPa)	4.54	2.26
G_D	(GPa)	2.72	1.33

the high-resolution density and V_S data are mainly constraining the results, whereas G_D results are dependent on S-wave velocity.

Monitor model results

In this second step, we consider that the reservoir frame properties are identified by the previous inversion on the baseline model and we want to invert only the saturation change. The a priori rock physics parameters are the solid phase (sands or shales) properties (bulk K_s and shear G_s moduli of grains and grains density ρ_s; see Table 2 and Figure 5d), the two fluid phases (water or gas) properties (fluid bulk moduli K_{f1} and K_{f2}, viscosities η_1 and η_2, and densities ρ_{f1} and ρ_{f2}; see Table 2) and the frame parameters obtained from the baseline data (ϕ, K_D, and G_D; see Figure 8 for inverted noise-free V_P data). We consider only the baseline results obtained from noise-free data with true V_S and ρ data in addition (Figure 8) which is the most favorable case. The results considering rock frame baseline models obtained from V_P only (Figure 7) and from noisy V_P data and true V_S and ρ (Figure 9) give similar results for the monitor model but are not shown here. We assume a V_P variation of 40 m/s in the two sand reservoirs. Using the effective fluid phase theory described before and by Dupuy et al. (2016b), we compute that these V_P changes correspond to a saturation in water equal to 4.2% for C3 reservoir (the big one on the right part of the Marmousi model) and 6.5% for C2 reservoir (small one on the left).

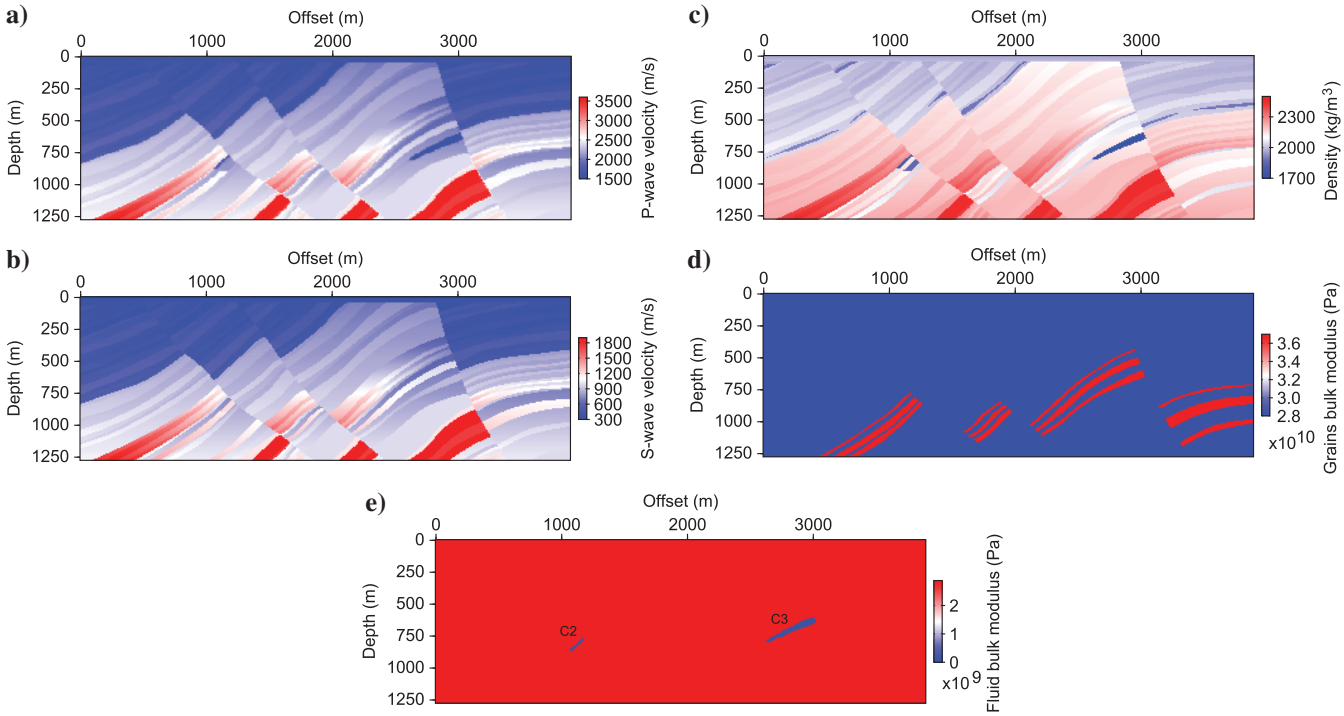

Figure 5. Viscoelastic and poroelastic true models: (a) V_P, (b) V_S, (c) ρ, (d) K_s, and (e) K_f. All the poroelastic properties (for grains and fluid phases) are given in Table 2. Here above are plotted only (d) the grains bulk modulus and (e) the fluid bulk modulus. For the grains (the other grains properties are given in Table 2), the blue zones stand for the sands layers and the red zones for the shales (d). For the fluid phase, the blue zones stand for the gas and the red zones for the water (the other fluid properties are given in Table 2). The reservoirs C2 and C3 are indicated in the bottom figure.

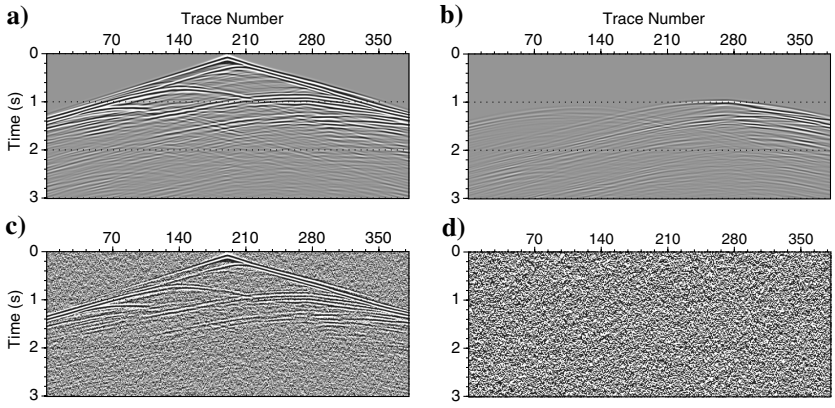

Figure 6. Seismograms for the source located at the center of Marmousi model (Asnaashari et al., 2015). (a) Noise-free baseline seismograms; (b) noise-free differential data between monitor and baseline data sets; (c) noisy baseline seismograms obtained with an artificial Gaussian band-limited noise in the bandwidth of source wavelet, which has been added to the noise-free data with S/N = 6 dB; (d) noisy differential data, the time-lapse seismic events are blinded by high level of random noise. Please note that the amplitude of the panels (b and d) seismograms are amplified by a factor of 10 for visualization purpose.

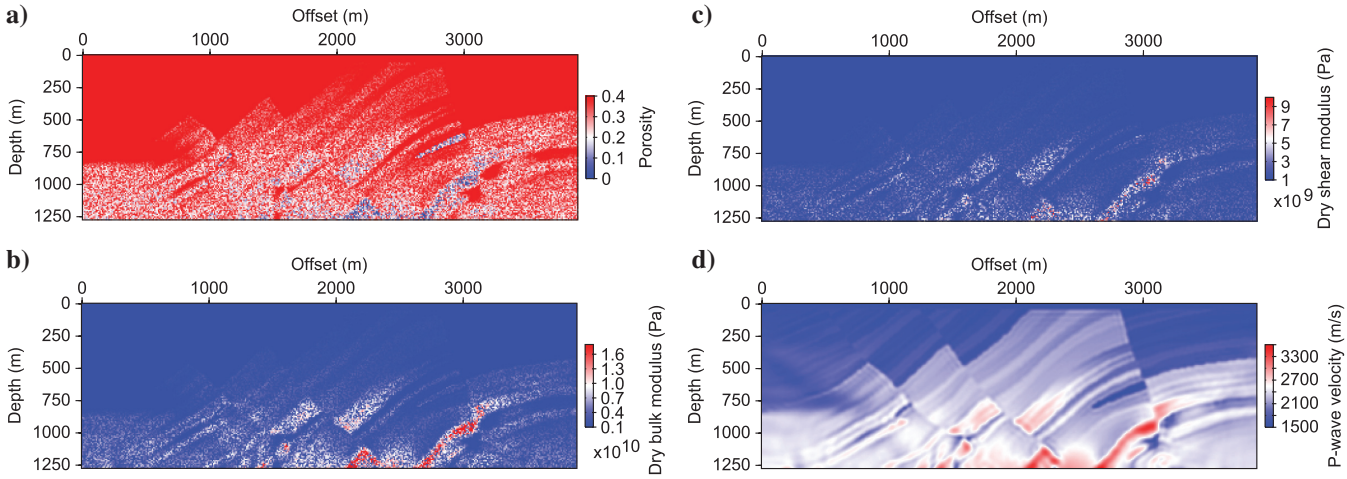

Figure 7. Inversion of frame poroelastic parameters ((a) ϕ, (b) K_D, and (c) G_D) from inverted V_P (d) (inverted from noise-free data; see Figure 6).

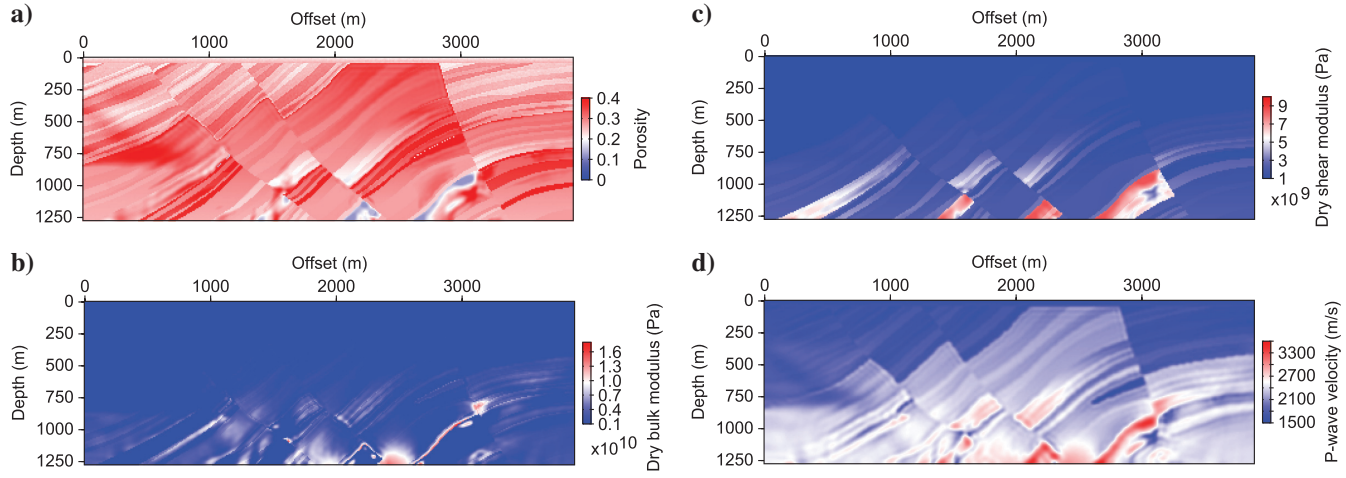

Figure 8. Inversion of frame poroelastic parameters ((a) ϕ, (b) K_D, and (c) G_D) from true V_S, true ρ and inverted V_P data (d) (inverted from noise-free data; see Figure 6).

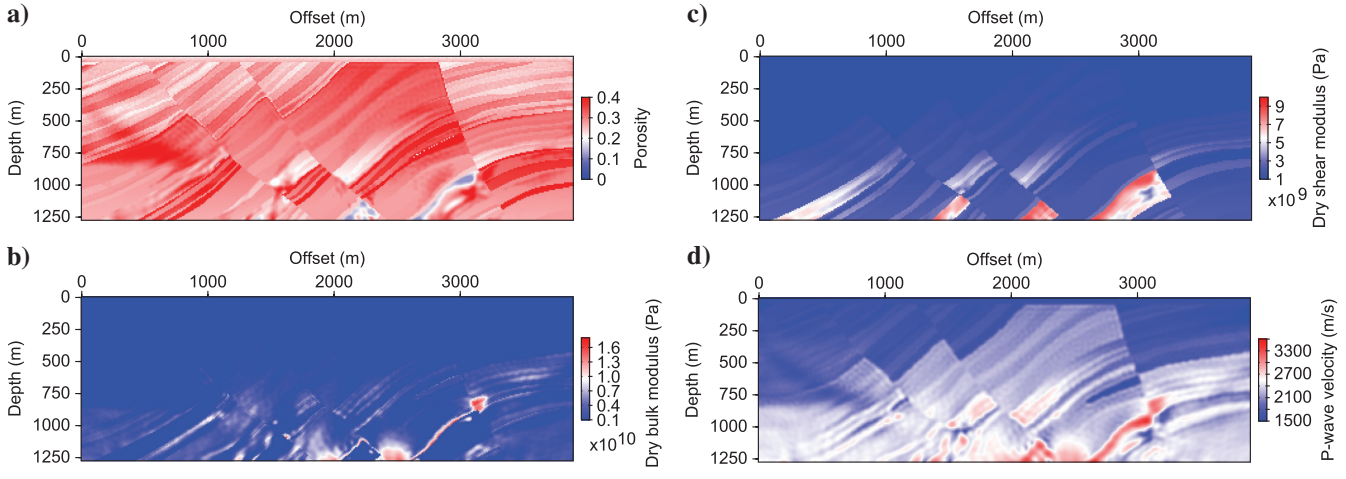

Figure 9. Inversion of frame poroelastic parameters ((a) ϕ, (b) K_D, and (c) G_D) from true V_S, true ρ and inverted V_P data (d) (inverted from noisy data; see Figure 6).

The obtained monitor and time-lapse variation results and the inverted water saturation are given in Figure 10 for noise-free and noisy data. We see that the obtained time-lapse result is quite better for noise-free data, but, as the order of magnitude of variation is low compared with the absolute value of V_P values, the monitor results are quite similar. Consequently, the poroelastic inversion results are similar whatever the noise in the data. Moreover, as the ϕ, K_D, and G_D inversion results are similar, we do not show the results for the three sets of baseline cases (Figures 7–9). Nevertheless, the monitor results considering the different frame properties are not very different and, consequently, are not highly dependent on the first-step inversion result. However, due to the point-by-point optimization method, the main part of the model (where there is no saturation change) is not well-determined. The extension of the saturation change is clearly identified by the poroelastic inversion, especially in the largest reservoir (right). However, the value of saturation is approximately well-recovered in the small reservoir ($3.2\% < V_1 < 17\%$, C2 on the left) but not in the large reservoir ($V_1 \simeq 1$, C3 on the right). It is probably due to the low amplitude of the V_P change compared with the V_P baseline values ($\Delta V_P = 40$ m/s and the initial $V_P = 2131$ m/s, i.e., 1.8% variation for C2 and $\Delta V_P = 40$ m/s and the initial $V_P = 1584$ m/s, i.e., 2.5% variation for C3) and because the water saturation is difficult to estimate using only P-wave velocity data (Dupuy et al., 2016b).

UNDERGROUND BLOWOUT IN THE NORTH SEA

The third example deals with North Sea time-lapse field data. An accidental underground blowout occurred in 1989 and developed in an exploration well during 326 days before being stopped by drilling a relief well. As a result, gas has migrated to shallower layers (Landrø, 2011). Repeated 2D lines were acquired as part of a site survey (the first one in 1988, the second one in 1990, one year after the blowout) (Zadeh and Landrø, 2011; Balhareth and Landrø, 2015). We ultimately aim at estimating the gas saturation and rock physics properties for a shallow sand layer (480 m deep) where gas has accumulated. Similar to the synthetic examples, we use a two-step inverse approach. First, we obtain the P-wave velocities (before and after the blowout) using FWI restricted to the acoustic case and applied in the time domain (Tarantola, 1984; Ratcliffe et al., 2011; Balhareth and Landrø, 2015). We estimate frame properties of the reservoir rocks using the baseline inverted velocity model, and then we estimate the gas saturation change using the monitor velocity model. However, contrary to synthetic examples, we do not have enough a priori information to carry out the rock physics inversion on the full model. Consequently, the inversion is focused on the reservoir which is the area of interest to estimate the gas saturation after the blowout. The gas saturation is estimated considering different partially saturated media theories. The first ones are related to the computation of an effective fluid phase plugged into the Biot-Gassmann theory, using different kinds of averages (Dupuy et al., 2016b). We also use the generalized patchy saturation theory using frequency-dependent moduli (Pride et al., 2004; Dupuy and Stovas, 2014) to take into account wave-induced fluid flow phenomena (Muller et al., 2010).

FWI results

The seismic data have been acquired on a seismic line that is 4.7 km long. The seismic acquisition geometry has source and

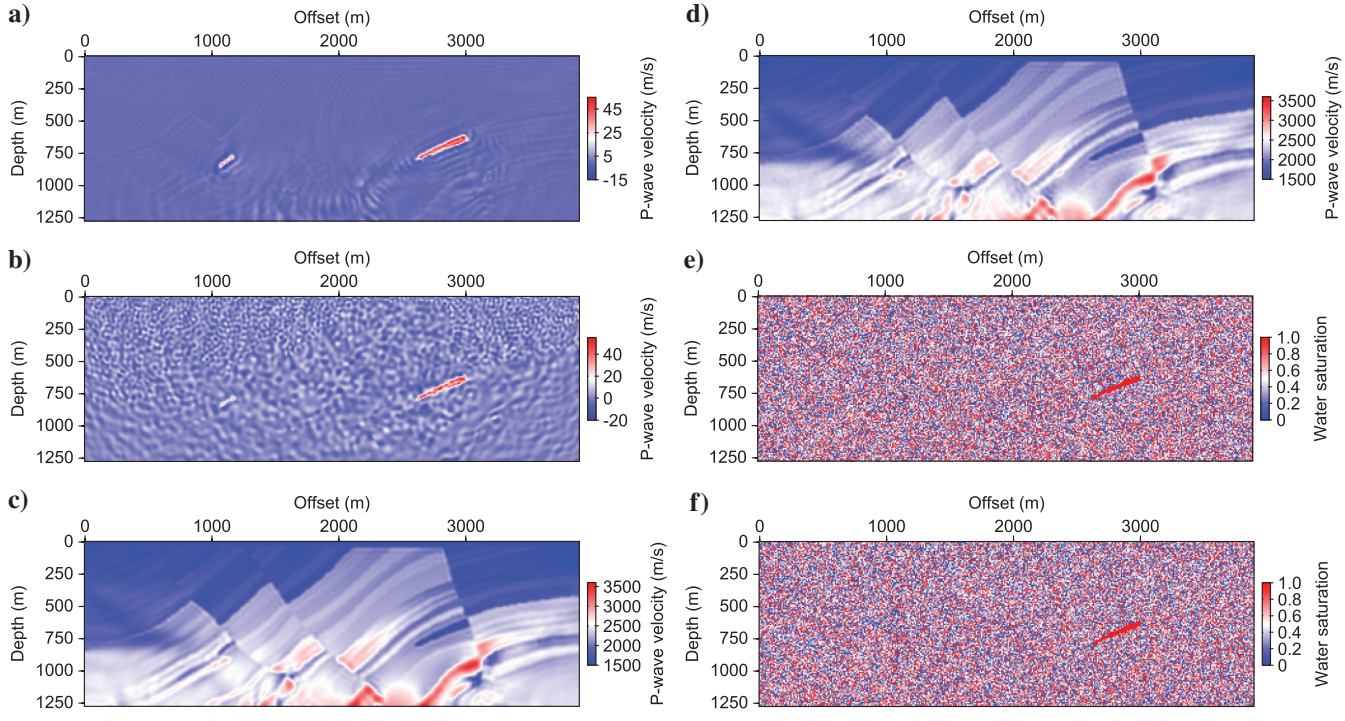

Figure 10. (a and b) Recovered time-lapse ΔV_P models, (c and d) recovered monitor V_P models obtained by double-difference inversion and (e and f) estimation of water saturation V_1 using a priori ϕ, K_D, and G_D data inverted without noise (baseline model, Figure 8). The results are given for (a, c, and e) noise-free seismic data and (b, d, and f) noisy seismic data.

receiver spacing of 12.5 m, with an offset range of 75–1250 m. The source is approximately 5 m deep. The field data quality is not optimal for FWI because a Butterworth filter was applied during acquisition which attenuated the low frequencies below 10 Hz. The maximum far offset is also relatively short (1250 m). However, the feasibility study (Balhareth and Landrø, 2015) showed that it is still possible to detect a shallow anomaly with the available nonoptimal seismic data. The FWI V_P results for baseline and monitor models and the differences between both are shown in Figure 11 (Balhareth and Landrø, 2015). The estimated V_P value for the baseline model is selected in the sand layer (480 m deep), whereas the velocity difference model gives the V_P changes around the well due to the gas accumulation in the sand layer. The V_P values used as input in the rock physics inversion process are extracted from the FWI results (computed at 12.5 Hz): Before blowout, the average value in the sand layer is $V_P = 1950$ m/s and we estimate the V_P change equal to 30−35 m/s. From the FWI image, the sand layer appears to be 40 m thick. However, the thickness is certainly lower, approximately 10–15 m (Langseth and Landrø, 2012) and this overestimation is probably due to the low vertical resolution of FWI. We can guess that only the 5–8 m top part is filled with gas, which means that the velocity change is smeared out quite strongly. The sensitivity analysis performed for this specific seismic data (Balhareth and Landrø, 2015) confirms that the FWI difference results are found to be underestimated by a factor of three due to smearing effect. Therefore, we choose $V_P = 1850$ m/s after the blowout (corresponding to a V_P change of approximately 100 m/s).

We assume that the grain properties correspond to quartz ($K_s = 39$ GPa, $G_s = 40$ GPa, and $\rho_s = 2690$ kg/m^3) and that the sand layer is saturated with water before the blowout ($K_{\text{fwater}} = 3$ GPa, $\eta_{\text{water}} = 0.001$ Pa.s, and $\rho_{\text{fwater}} = 1040$ kg/m^3) and partially saturated with gas and water after the blowout ($K_{\text{fgas}} = 0.1$ GPa, $\eta_{\text{gas}} = 0.00004$ Pa.s, and $\rho_{\text{fgas}} = 310$ kg/m^3). The sensitivity tests (Dupuy et al., 2016b) confirm that the permeability k_0 and the cementation factor m do not have significant influence on inversion results, so we choose $k_0 = 10^{-12}$ m^2 and $m = 1$.

Baseline model results

To determine the reservoir rock properties, we invert the porosity ϕ, the bulk dry modulus K_D, and the shear dry modulus G_D for the baseline data. The results are given in Figure 12. The best (with the lowest misfit value) model is $\phi = 0.454$, $K_D = 1.7$ GPa, and $G_D = 0.12$ GPa. It is important to note that the ranges (as shown in Figure 12) of $0.325 < \phi < 0.5$, 0.2 GPa $< K_D < 2$ GPa, and 0.1 GPa $< G_D < 1$ GPa give acceptable results (with respect to a misfit lower than 0.1%, so a V_P fitting less than 2 m/s). On the other hand, the three rock frame properties are coupled and affect the P-wave velocity. Consequently, we choose three different reservoir models from three local minima, with porosity between 0.35 and 0.45, to have a better description of the possible solutions:

- reservoir 1 (best model): $\phi = 0.454$, $K_D = 1.7$ GPa, and $G_D = 0.12$ GPa,
- reservoir 2: $\phi = 0.3997$, $K_D = 0.503$ GPa, and $G_D = 0.533$ GPa, and
- reservoir 3: $\phi = 0.3456$, $K_D = 0.523$ GPa, and $G_D = 0.157$ GPa.

Monitor model results

We assume that the gas appearance is the only change during the blowout, and then we consider that, in the sand layer reservoir, the medium becomes saturated with gas and water, so that we invert only the gas saturation. If we use the patchy saturation theory (White, 1975), we obtain a gas saturation equal to 0.57%, whereas the gas saturation is equal to 3.3% if we use an effective fluid phase (Brie et al. [1995] average with $e = 5$ for the bulk modulus). Because we have only one unknown in the rock physics inversion, we can plot V_P with respect to the saturation in Figure 13a for Brie average and patchy saturation models flanked by low and high bounds. The patchy saturation results are very close to the Reuss low bound theory. V_P variations with respect to the saturation for the three different reservoir rocks are also plotted in Figure 13b. We see that the reservoir properties do not have a strong influence

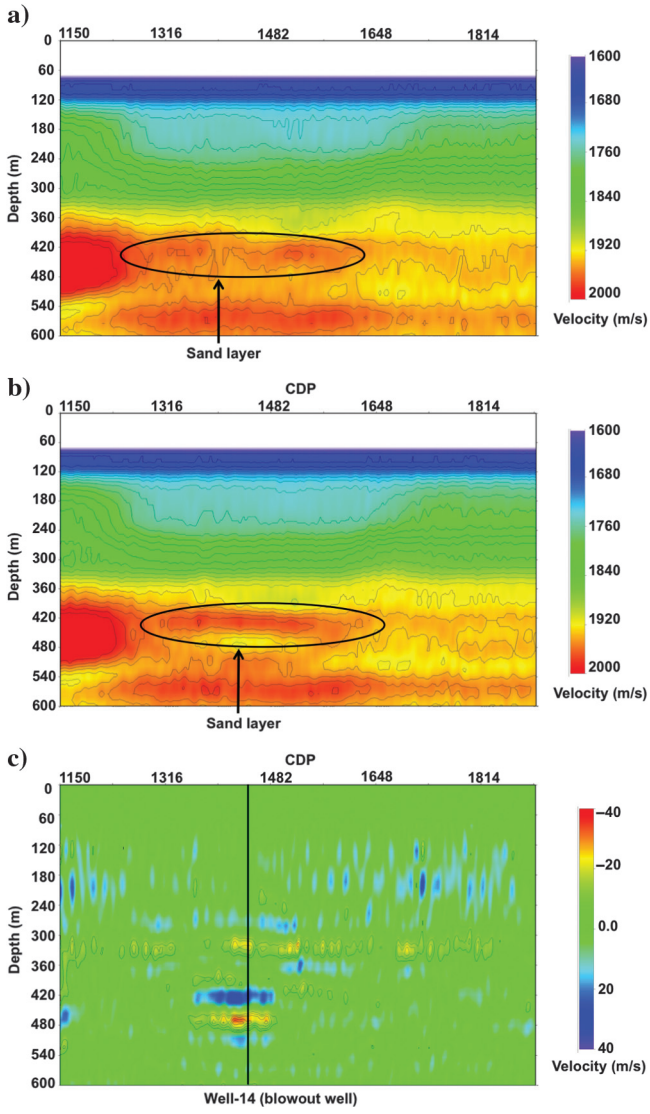

Figure 11. P-wave velocity FWI result. (a) Baseline, (b) monitor, and (c) differences models. The 480 m deep anomaly (sand layer) and the position of the blowout well are indicated.

on the results: The gas saturation is equal to approximately 3% for Brie averages and 0.6% for patchy saturation.

DISCUSSION

The three different applications confirm the observations of the sensitivity tests (Dupuy et al., 2016b), especially for the field data case, i.e., that the rock physics inversion system should be well-determined to obtain accurate results. For the synthetic tests, the results are conclusive but the FWI input data allow to be in a favorable case. Indeed, for the baseline model, the quality of the rock physics inversion depends only on the quality of acoustic FWI results. The first test case show that we can recover accurately the porosity from P-wave velocity obtained with acoustic FWI. In the monitor model, the fluid bulk modulus is approximately well-recovered and allows to determine the fluid type but the two other fluid properties are poorly estimated because P-wave velocity is weakly sensitive to viscosity and fluid density (and, in addition, the system is underdetermined). The second synthetic test shows that including S-wave velocity and density data help to constrain the inversion of the three rock frame parameters. In the monitor model, the saturation is difficult to estimate correctly using only V_P data, while it is shown in the sensitivity tests that it requires attenuation data (Dupuy et al., 2016b). However, the monitor model results are not strongly dependent on the uncertainty of the baseline rock frame estimations. When the rock physics inversion is not converging toward homogeneous results, pixel patterns appear due to the local minima. Including additional a priori information should improve the results. It is also possible to implement a spatial smoothing term directly in the cost function to establish spatial correlation between pixels (Moyano et al., 2015). Nevertheless, the estimation of the correlation length is an ongoing problem, the poroelastic medium being described at the microscale, whereas an intermediate mesoscale is defined for effective medium and the viscoelastic attributes are sensitive to macroscale properties (Dupuy et al., 2016a). The seismic waves are then affected by macroscale objects but these objects can hold mesoscale variations that will affect the macroscale behavior (Muller et al., 2010).

For the field data case, we are also limited to acoustic FWI results. Before the blowout, we obtain a range of acceptable values and we choose three sets of values with porosities between 0.35 and 0.45. Then, the time-lapse FWI V_P changes allow to estimate the gas saturation, between 0.5% and 3.5% depending on the partial saturation theory which is chosen. The porosity of the reservoir rock (and the associated moduli) does not have a strong influence on this saturation estimation. Moreover, the uncertainties on FWI results, on input rock physics parameters (K_f of gas and water may have influence on gas saturation estimation), and on the rock physics models themselves (the gas saturation value may reach the Voigt upper bound and be approximately 20%) can be the cause of an underestimation of the gas saturation in the sand layer. Indeed, pressure-saturation changes estimation of Bhakta and Landrø (2014) (using AVO data for the same blowout case) gives gas saturation values between 10% and 45% and pore pressure changes of the order of 1.6–2.8 MPa. Using 2D time-lapse seismic data coupled with reservoir simulation, Langseth and Landrø (2012) estimate that the gas saturation is approximately 35%–40% and the pore pressure approximately 9 MPa.

An additional issue in the field data case is that we have used two independent FWI instead of differential time-lapse strategy because it is done in synthetic examples. The difference of two independent FWI results is able to recover the time-lapse changes as well. However, this strategy cannot focus only on the area of actual time-lapse changes. Because the two independent inversions are performed separately, the paths of convergence might not be the same for both FWI. Therefore, a subtraction between two final models may show changes in other areas which are not affected by the gas saturation change only and could be the cause of the inversion artifacts observed on the field data case (the velocity change is strongly smeared out). The double-difference strategy, due to focusing on the difference data and starting the time-lapse inversion from an already-reconstructed baseline model, does not much suffer from the issue mentioned above. Asnaashari et al. (2015) find that the differ-

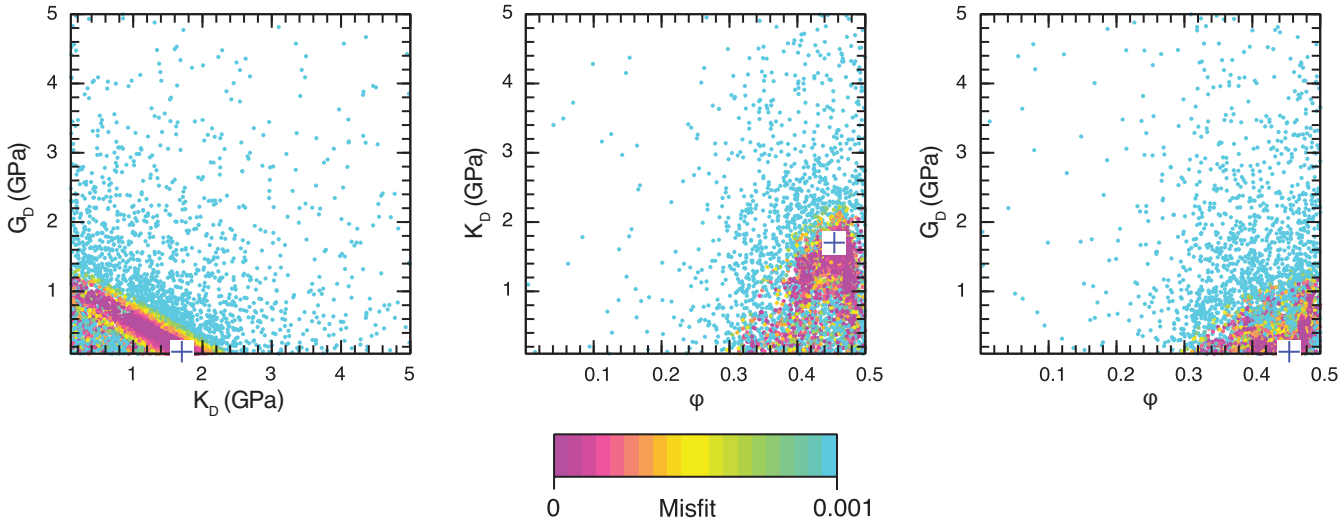

Figure 12. Inversion results for baseline model (before blowout). We give the results of the estimation of the porosity ϕ, the dry bulk modulus K_D, and the dry shear modulus G_D in 2D slices of the 3D parameters space (ϕ, K_D, and G_D). The dot color depends on the misfit value (each dot is a model) which is given in absolute value, namely between 0% and 0.1%. The best estimated model is represented by the blue cross.

ential time-lapse strategy can deliver more robust, more accurate and more clear time-lapse variation image. In addition, the joint time-lapse inversion (proposed by Maharramov and Biondi, 2015), in which the baseline and the difference signal are inverted simultaneously would probably be a better option. Applying these time-lapse strategies to field data would probably help to obtain a better estimation of gas saturation, but this requires specific permanent acquisition systems to have perfect data repeatability.

The increase of pore pressure (due to gas accumulation in the sealed sand layer) is not considered in our rock physics inversion. The leakage in the sand layer causes the increase of the saturation and the pore pressure and both effects are combined to decrease the P-wave velocity (the pore pressure increase causes a lower coupling between grains and a decrease in effective stress [Bhakta and Landrø, 2014]). Because we have considered only the gas saturation change, our results are probably overestimated. Nevertheless, we can assume that the pore pressure effect is low because our estimation is already lower than those of Langseth and Landrø (2012) and Bhakta and Landrø (2014). Moreover, we think that the saturation in this highly porous sand layer is likely uniform, and promote the estimation using Brie equation (Figure 13), that bring up the estimation of 3%–4% of gas. The use of V_S data can be a good way to discriminate saturation and pressure effects, the S-waves being more sensitive to solid phase changes (pore pressure) than to fluid phases changes (saturation). However, as Biot (1956a, 1956b), equations do not involve any effective pressure terms, considering pore pressure effects require the use of empirical approximated relations (Landrø, 2001; Grude et al., 2014). On the other hand, due to the blowout (or the injection), some compaction and, consequently, some porosity changes can occur between monitor and baseline stages (due to a change in stresses or chemical reactions). In this case, it could be required to invert jointly porosity and saturation for the monitor data.

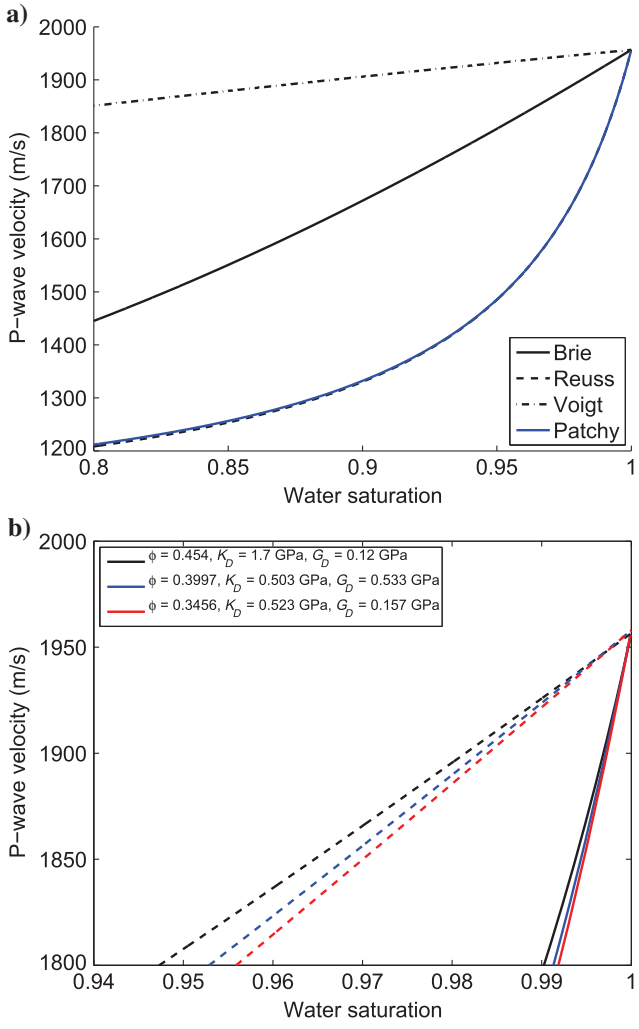

Figure 13. P-wave velocity with respect to the water saturation. (a) Based on reservoir 1: effective fluid phase model (Brie uniform saturation with $e = 5$) in black continuous lines, Reuss lower bound in black dashed lines, Voigt upper bound in black dotted-dashed lines, and patchy saturation in blue continuous lines. (b) Several reservoir rocks models: Brie uniform saturation in dashed lines and patchy saturation in continuous lines. Reservoir 1 in black lines, reservoir 2 in blue lines, and reservoir 3 in red lines.

Besides the critical use of S-wave input data, the potential improvements of poroelastic estimations are numerous. The use of other parameter settings should be investigated as impedances or logarithmic functions. The use of additional data on amplitude (AVO) could give more information about wave amplitude and help to constrain the saturation estimation (Dupuy and Stovas, 2014). Considering frequency dispersion may lead to a major improvement, taking into account the strong dispersion of seismic waves that can occur with wave-induced fluid flow phenomena at seismic frequencies (Muller et al., 2010) and adding more data to the inversion. Indeed, the viscoelastic properties (velocities and attenuations) are extracted at a given frequency (the highest frequency used for the FWI step). The use of dynamic poroelastic models (taking into account this frequency dependence) is crucial for highly dispersive reservoir problems (partial saturation) or log data applications. While Gassmann's relation (Gassmann, 1951) is a low-frequency approximation, considering accurately the dispersion (and the frequency dependence of the quality factors) in the dynamic poroelastic model (Pride, 2005) can allow us to mix several velocities inputs (log data plus FWI) with different frequency content. Mostly, as said previously, the availability of S-waves and attenuation input data is crucial for poroelastic estimations and it is consequently promoting the FWI effort toward multiparameter inversions. Finally, considering other geophysical data as controlled-source electromagnetic (CSEM) (Bhuyian et al., 2012) or gravity (Alnes et al., 2008; Stenvold et al., 2008) can bring additional information about underground fluids and could be used in jointly inversions (Hoversten et al., 2006; Gao et al., 2012).

CONCLUSIONS

In this work, we have developed a workflow to estimate poroelastic parameters from seismograms. We propose a two-step strategy, consisting of high-resolution quantitative seismic imaging (FWI) and followed by a rock physics inversion process. This approach is based on analytical Biot-Gassmann equations combined with generalized dynamic permeability to build an effective porous medium. The poroelastic inverse problem is solved using a semi-global optimization method (NA algorithm). We applied this strategy to three different 2D acoustic cases in which fluid substitution is concerned. The synthetic steam injection monitoring case shows that the quality of inversion depends on the quality of V_P estimations. The poroelastic inversion gives a good estimation of the

porosity from V_P data for baseline model, whereas fluid bulk modulus changes are well-recovered from V_P time-lapse data. The time-lapse monitoring of the Marmousi model gives nice results for the rock frame properties estimation (baseline model) but require the use of elastic inputs. The estimation of the water saturation using acoustic FWI monitor results is difficult because the signature of the saturation on the P-wave velocity is weak. The field data case sums up at the same time the challenges and the promises of the proposed method. Even with the limited nature of input data with an acoustic approach (only V_P data), we are able to estimate the rock frame parameters. In addition, the following estimation on saturation (based on the velocity change) is weakly dependent on the frame properties estimation. However, due to the limited data availability and due to the uncertainties on a priori parameters and the crucial choice of rock physics models, the estimation of gas saturation is not accurate, ranging between 0.6% and 5% if we consider conventional partial saturation models. In this real-data case, it appears necessary to use various seismic attributes, and FWI effort should be conducted toward multiparameter inversion.

ACKNOWLEDGMENTS

We would like to thank M. Sambridge for providing his neighborhood algorithm code used in this paper. B. Dupuy thanks the ANR "Captage et Stockage de CO_2" program (ANR-07-PCO2-002) and the Norwegian Research Council and the other sponsors of the ROSE project at NTNU for financial support. H. Balhareth thanks Saudi Aramco for funding his Ph.D. and CGG Veritas for giving access to use their FWI software. The companies financing the LOSEM Consortium (Bayern Gas, BP, Det Norske, Petrobras, Lundin Petroleum, Statoil, and Total) are acknowledged. We are also grateful to two anonymous reviewers, M. Maharramov and to the associate editor A. Guitton for their constructive comments.

REFERENCES

Alnes, H., O. Eiken, and T. Stenvold, 2008, Monitoring gas production and CO_2 injection at the Sleipner field using time-lapse gravimetry: Geophysics, **73**, no. 6, WA155–WA161, doi: 10.1190/1.2991119.

Asnaashari, A., R. Brossier, S. Garambois, F. Audebert, P. Thore, and J. Virieux, 2011, Sensitivity analysis of time-lapse images obtained by differential waveform inversion with respect to reference model: 81st Annual International Meeting, SEG, Expanded Abstracts, 2482–2486.

Asnaashari, A., R. Brossier, S. Garambois, F. Audebert, P. Thore, and J. Virieux, 2013, Regularized seismic full waveform inversion with prior model information: Geophysics, **78**, no. 2, R25–R36, doi: 10.1190/geo2012-0104.1.

Asnaashari, A., R. Brossier, S. Garambois, F. Audebert, P. Thore, and J. Virieux, 2015, Time-lapse seismic imaging using regularized full waveform inversion with prior model: Which strategy?: Geophysical Prospecting, **63**, 78–98, doi: 10.1111/gpr.2015.63.issue-1.

Avseth, P., T. Mukerji, and G. Mavko, 2005, Quantitative seismic interpretation: Applying rock physics tools to reduce interpretation risk: Cambridge University Press.

Balhareth, H. M., and M. Landrø, 2015, Sensitivity analysis and application of the time-lapse full waveform inversion: Synthetic testing, and field data example from the North Sea, Norway: Geophysical Prospecting.

Batzle, M., and Z. Wang, 1992, Seismic properties of pore fluids: Geophysics, **57**, 1396–1408, doi: 10.1190/1.1443207.

Berkhout, A. J., and C. P. A. Wapenaar, 1990, Delphi: Delft philosophy on acoustic and elastic inversion: The Leading Edge, **9**, 30–33, doi: 10.1190/1.1439716.

Berryman, J., P. Berge, and B. Bonner, 2002, Estimating rock porosity and fluid saturation using only seismic velocities: Geophysics, **67**, 391–404, doi: 10.1190/1.1468599.

Bhakta, T., and M. Landrø, 2014, Estimation of pressure-saturation changes for unconsolidated reservoir rocks with high V_P/V_S ratio: Geophysics, **79**, no. 5, M35–M54, doi: 10.1190/geo2013-0434.1.

Bhuyian, A. H., M. Landrø, and S. E. Johansen, 2012, 3D CSEM modeling and time-lapse sensitivity analysis for subsurface CO_2 storage: Geophysics, **77**, no. 5, E343–E355, doi: 10.1190/geo2011-0452.1.

Biot, M., 1956a, Theory of propagation of elastic waves in a fluid-saturated porous solid. I. Low-frequency range: Journal of Acoustical Society of America, **28**, 168–191, doi: 10.1121/1.1908239.

Biot, M., 1956b, Theory of propagation of elastic waves in a fluid-saturated porous solid. II. Higher frequency range: Journal of Acoustical Society of America, **28**, 168–191, doi: 10.1121/1.1908239.

Bourbié, T., O. Coussy, and B. Zinszner, 1986, Acoustique des milieux poreux: Institut Francais du pétrole 27.

Brie, A., F. Pampuri, A. Marsala, and O. Meazza, 1995, Shear sonic interpretation in gas-bearing sands: Presented at the SPE Annual Technical Conference 30595, 701–710.

Brossier, R., S. Operto, and J. Virieux, 2009, Seismic imaging of complex onshore structures by 2D elastic frequency-domain full-waveform inversion: Geophysics, **74**, no. 6, WCC105–WCC118, doi: 10.1190/1.3215771.

Choi, Y., D. Min, and C. Shin, 2008, Two-dimensional waveform inversion of multi-component data in acoustic-elastic coupled media: Geophysical Prospecting, **56**, 863–881, doi: 10.1111/gpr.2008.56.issue-6.

Chotiros, N., 2002, An inversion for Biot parameters in a water-saturated sand: Journal of Acoustical Society of America, **112**, 1853–1868, doi: 10.1121/1.1511199.

Dai, N., A. Vafidis, and E. Kanasewich, 1995, Wave propagation in heterogeneous porous media: A velocity-stress, finite-difference method: Geophysics, **60**, 327–340, doi: 10.1190/1.1443769.

De Barros, L., and M. Dietrich, 2008, Perturbations of the seismic reflectivity of a fluid-saturated depth-dependent poroelastic medium: Journal of Acoustical Society of America, **123**, 1409–1420, doi: 10.1121/1.2835419.

De Barros, L., M. Dietrich, and B. Valette, 2010, Full waveform inversion of seismic waves reflected in a stratified porous medium: Geophysical Journal International, **182**, 1543–1556, doi: 10.1111/j.1365-246X.2010.04696.x.

Denli, H., and L. Huang, 2009, Double-difference elastic waveform tomography in the time domain: 79th Annual International Meeting, SEG, Expanded Abstracts, 2302–2306.

Dupuy, B., A. Asnaashari, R. Brossier, S. Garambois, L. Metivier, A. Ribodetti, and J. Virieux, 2016a, A downscaling strategy from FWI to microscale reservoir properties from high-resolution images: The Leading Edge, **35**, 146–150, doi: 10.1190/tle35020146.1.

Dupuy, B., L. De Barros, S. Garambois, and J. Virieux, 2011, Wave propagation in heterogeneous porous media formulated in the frequency-space domain using a discontinuous Galerkin method: Geophysics, **76**, no. 4, N13–N28, doi: 10.1190/1.3581361.

Dupuy, B., S. Garambois, and J. Virieux, 2016b, Estimation of rock physics properties from seismic attributes. Part 1: Strategy and sensitivity analysis: Geophysics, **81**, no. 3, M35–M53, doi: 10.1190/geo2015-0239.1.

Dupuy, B., and A. Stovas, 2014, Influence of frequency and saturation on AVO attributes for patchy saturated rocks: Geophysics, **79**, no. 1, B19–B36, doi: 10.1190/geo2012-0518.1.

Forgues, E., and G. Lambaré, 1997, Parameterization study for acoustic and elastic ray + Born inversion: Journal of Seismic Exploration, **6**, 253–278.

Gao, G., A. Abubakar, and T. M. Habashy, 2012, Joint petrophysical inversion of electromagnetic and full-waveform seismic data: Geophysics, **77**, no. 3, WA3–WA18, doi: 10.1190/geo2011-0157.1.

Gassmann, F., 1951, Über die Elastizität poröser Medien: Vierteljahrsschrift der Naturforschenden Gesellschaft in Zurich, **96**, 1–23.

Gosselet, A., and S. Singh, 2008, 2D full wave form inversion in time-lapse mode: CO_2 quantification at Sleipner: 70th Annual International Conference and Exhibition, EAGE, Extended Abstracts, W075.

Grude, S., M. Landrø, and J. Dvorkin, 2014, Pressure effects caused by CO_2 injection in the Tubaen Fm., the Snohvit field: International Journal of Greenhouse Gas Control, **27**, 178–187, doi: 10.1016/j.ijggc.2014.05.013.

Hicks, G. J., and R. G. Pratt, 2001, Reflection waveform inversion using local descent methods: Estimating attenuation and velocity over a gas-sand deposit: Geophysics, **66**, 598–612, doi: 10.1190/1.1444951.

Hoversten, G. M., F. Cassassuce, E. Gasperikova, G. A. Newman, J. Chen, Y. Rubin, Z. Hou, and D. Vasco, 2006, Direct reservoir parameter estimation using joint inversion of marine seismic AVA and CSEM data: Geophysics, **71**, no. 3, C1–C13, doi: 10.1190/1.2194510.

Johansen, T. A., E. H. Jensen, G. Mavko, and J. Dvorkin, 2013, Inverse rock physics modeling for reservoir quality prediction: Geophysics, **78**, no. 2, M1–M18, doi: 10.1190/geo2012-0215.1.

Johnson, D., J. Koplik, and R. Dashen, 1987, Theory of dynamic permeability and tortuosity in fluid-saturated porous media: Journal of Fluid Mechanics, **176**, 379–402, doi: 10.1017/S0022112087000727.

Kamei, R., and R. G. Pratt, 2013, Inversion strategies for visco-acoustic waveform inversion: Geophysical Journal International, **194**, 859–884, doi: 10.1093/gji/ggt109.

Landrø, M., 2001, Discrimination between pressure and fluid saturation changes from time-lapse seismic data: Geophysics, **66**, 836–844, doi: 10.1190/1.1444973.

Landrø, M., 2011, Seismic monitoring of an old underground blowout — 20 years later: First Break, **29**, 39–48.

Langseth, E., and M. Landrø, 2012, Time-lapse 2D interpretation of gas migration in shallow sand layers — Compared to reservoir simulation: International Journal of Greenhouse Gas Control, **10**, 389–396, doi: 10.1016/j.ijggc.2012.07.007.

Levander, A. R., 1988, Fourth-order finite-difference P-SV seismograms: Geophysics, **53**, 1425–1436, doi: 10.1190/1.1442422.

Liao, O., and G. A. McMechan, 1995, 2.5D full-wavefield viscoacoustic inversion: Geophysical Prospecting, **43**, 1043–1059, doi: 10.1111/gpr.1995.43.issue-8.

Maharramov, M., and B. Biondi, 2015, Robust simultaneous time-lapse full-waveform inversion with total-variation regularization of model difference: 77th Annual International Conference and Exhibition, EAGE, Extended Abstracts, We P3 09.

Malinowski, M., S. Operto, and A. Ribodetti, 2011, High-resolution seismic attenuation imaging from wide-aperture onshore data by visco-acoustic frequency-domain full waveform inversion: Geophysical Journal International, **186**, 1179–1204, doi: 10.1111/j.1365-246X.2011.05098.x.

Martin, G. S., R. Wiley, and K. J. Marfurt, 2006, Marmousi2: An elastic upgrade for Marmousi: The Leading Edge, **25**, 156–166, doi: 10.1190/1.2172306.

Mavko, G., T. Mukerji, and J. Dvorkin, 2009, The rocks physics handbooks, tools for seismic analysis in porous media (2nd ed.): Cambridge University Press.

Mora, P. R., 1987, Nonlinear two-dimensional elastic inversion of multi-offset seismic data: Geophysics, **52**, 1211–1228, doi: 10.1190/1.1442384.

Mora, P. R., 1989, Inversion = migration + tomography: Geophysics, **54**, 1575–1586, doi: 10.1190/1.1442625.

Morency, C., Y. Luo, and J. Tromp, 2009, Finite-frequency kernels for wave propagation in porous media based upon adjoint methods: Geophysical Journal International, **179**, 1148–1168, doi: 10.1111/gji.2009.179.issue-2.

Moyano, B., E. H. Jensen, and T. A. Johansen, 2015, Spatial constrained inverse rock physics modelling: Geophysical Prospecting, **63**, 183–191, doi: 10.1111/gpr.2015.63.issue-1.

Muller, T., B. Gurevich, and M. Lebedev, 2010, Seismic wave attenuation and dispersion resulting from wave-induced flow in porous rocks — A review: Geophysics, **75**, no. 5, 75A147–75A164, doi: 10.1190/1.3463417.

Operto, S., Y. Gholami, V. Prieux, A. Ribodetti, R. Brossier, L. Metivier, and J. Virieux, 2013, A guided tour of multiparameter full-waveform inversion with multicomponent data: From theory to practice: The Leading Edge, **39**, 1040–1054, doi: 10.1190/tle32091040.1.

Plessix, R. E., S. Michelet, H. Rynja, H. Kuehl, C. Perkins, J. W. de Maag, and P. Hatchell, 2010, Some 3D applications of full waveform inversion: 72nd Annual International Conference and Exhibition, EAGE, Extended Abstracts, W608.

Pride, S., 2005, Hydrogeophysics: Springer, Water Science and Technology Library, 253–284.

Pride, S., J. Berryman, and J. Harris, 2004, Seismic attenuation due to wave-induced flow: Journal of Geophysical Research, **109**, 1–19.

Prieux, V., R. Brossier, S. Operto, and J. Virieux, 2013a, Multiparameter full waveform inversion of multicomponent ocean-bottom-cable data from the Valhall field. Part 1: Imaging compressional wave speed, density and attenuation: Geophysical Journal International, **194**, 1640–1664, doi: 10.1093/gji/ggt177.

Prieux, V., R. Brossier, S. Operto, and J. Virieux, 2013b, Multiparameter full waveform inversion of multicomponent ocean-bottom-cable data from the Valhall field. Part 2: Imaging compressive-wave and shear-wave velocities: Geophysical Journal International, **194**, 1665–1681, doi: 10.1093/gji/ggt178.

QueiBer, M., and S. C. Singh, 2013, Full waveform inversion in the time lapse mode applied to CO_2 storage at Sleipner: Geophysical Prospecting, **61**, 537–555, doi: 10.1111/gpr.2013.61.issue-3.

Qureshi, T., M. Kleemeyer, B. Blonk, R. van der Weiden, and Z. Rujie, 2012, The benefits of low frequencies in seismic inversion: A land example: Presented at the 9th Biennial International Conference and Exposition on Petroleum Geophysics.

Raknes, E. B., B. Arntsen, and W. Weibull, 2015, Three-dimensional elastic full waveform inversion using seismic data from the Sleipner area: Geophysical Journal International, **202**, 1877–1894, doi: 10.1093/gji/ggv258.

Ratcliffe, A., C. Win, V. Vinje, G. Conroy, M. Warner, A. Umpleby, I. Stekl, T. Nangoo, and A. Bertrand 2011, Full waveform inversion: A North Sea OBC case study: 81st Annual International Meeting, SEG, Expanded Abstracts, 2384–2388.

Ren, Z., and Y. Liu, 2015, Elastic full-waveform inversion using the second-generation wavelet and an adaptive-operator-length scheme: Geophysics, **80**, no. 4, R155–R173, doi: 10.1190/geo2014-0516.1.

Ren, Z., Y. Liu, and Q. Zhang, 2014, Multiscale viscoacoustic waveform inversion with the second generation wavelet transform and adaptive time-space domain finite-difference method: Geophysical Journal International, **197**, 948–974, doi: 10.1093/gji/ggu024.

Ribodetti, A., S. Operto, J. Virieux, G. Lambaré, H.-P. Valéro, and D. Gibert, 2000, Asymptotic viscoacoustic diffraction tomography of ultrasonic laboratory data: A tool for rock properties analysis: Geophysical Journal International, **140**, 324–340, doi: 10.1046/j.1365-246x.2000.00015.x.

Romdhane, A., G. Grandjean, R. Brossier, F. Rejiba, S. Operto, and J. Virieux, 2011, Shallow-structure characterization by 2D elastic full-waveform inversion: Geophysics, **76**, no. 3, R81–R93, doi: 10.1190/1.3569798.

Romdhane, A., and E. Querendez, 2014, CO_2 characterization at the Sleipner field with full waveform inversion: Application to synthetic and real data: Energy Procedia, **63**, 4358–4365, doi: 10.1016/j.egypro.2014.11.470.

Saltzer, R., C. Finn, and O. Burtz, 2005, Predicting V_{shale} and porosity using cascaded seismic and rock physics inversion: The Leading Edge, **24**, 732–736, doi: 10.1190/1.1993269.

Sambridge, M. S., 1999, Geophysical inversion with a neighbourhood algorithm — I: Searching a parameter space: Geophysical Journal International, **138**, 479–494, doi: 10.1046/j.1365-246X.1999.00876.x.

Sears, T., S. Singh, and P. Barton, 2008, Elastic full waveform inversion of multi-component OBC seismic data: Geophysical Prospecting, **56**, 843–862, doi: 10.1111/gpr.2008.56.issue-6.

Shi, Y., W. Zhao, and H. Cao, 2007, Nonlinear process control of wave-equation inversion and its application in the detection of gas: Geophysics, **72**, no. 1, R9–R18, doi: 10.1190/1.2399450.

Sirgue, L., O. I. Barkved, J. P. V. Gestel, O. J. Askim, and J. H. Kommedal, 2009, 3D waveform inversion on Valhall wide-azimuth OBC: 71st Annual International Conference and Exhibition, EAGE, Extended Abstracts, U038.

Sirgue, L., and R. G. Pratt 2004, Efficient waveform inversion and imaging: A strategy for selecting temporal frequencies: Geophysics, **69**, 231–248, doi: 10.1190/1.1649391.

Stenvold, T., O. Eiken, and M. Landrø, 2008, Gravimetric monitoring of gas-reservoir water influx — A combined flow- and gravity-modeling approach: Geophysics, **73**, no. 6, WA123–WA131, doi: 10.1190/1.2991104.

Tarantola, A., 1984, Inversion of seismic reflection data in the acoustic approximation: Geophysics, **49**, 1259–1266, doi: 10.1190/1.1441754.

Tarantola, A., 1986, A strategy for non linear inversion of seismic reflection data: Geophysics, **51**, 1893–1903, doi: 10.1190/1.1442046.

Teja, A., and P. Rice, 1981, Generalized corresponding states method for viscosities of liquid mixtures: Industrial and Engineering Chemistry Fundamentals, **20**, 77–81, doi: 10.1021/i100001a015.

Watanabe, T., S. Shimizu, E. Asakawa, and T. Matsuoka, 2004, Differential waveform tomography for time-lapse crosswell seismic data with application to gas hydrate production monitoring: 74th Annual International Meeting, SEG, Expanded Abstracts, 2323–2326, doi: 10.1190/SEGEAB.23.

White, J. E., 1975, Computed seismic speeds and attenuation in rocks with partial gas saturation: Geophysics, **40**, 224–232, doi: 10.1190/1.1440520.

Zadeh, H. M., and M. Landrø, 2011, Monitoring a shallow subsurface gas flow by time-lapse refraction analysis: Geophysics, **76**, no. 6, O35–O43, doi: 10.1190/geo2011-0012.1.